

Strength-plasticity synergy from ambient to high temperature via gradient-ordering in boride-reinforced WTaV medium-entropy alloy

Received: 21 February 2025

Accepted: 11 November 2025

Published online: 21 November 2025

 Check for updatesBo Sun^{1,2,6}, Bingjie Wang^{1,2,6}, Zhe Jia^{1,2}, Ligang Sun³, Juan Kuang^{1,2}, Qianqian Wang^{1,2}✉, Gang Sha⁴, Xiubing Liang⁵✉ & Baolong Shen^{1,2}✉

Developing next-generation hypersonic vehicles necessitates structural materials capable of withstanding extreme thermal gradients. However, conventional alloys usually sacrifice room-temperature plasticity for breakthroughs in high-temperature strength. Here, we report a (WTaV)₉₀B₁₀ refractory medium-entropy alloy (RMEA) that overcomes this trade-off, showing decent plasticity of ~6% at ambient temperature, high yield strength of 650 MPa at 1873 K and 242 MPa at 2073 K, and excellent thermal stability up to ~0.7 T_m . The RMEA comprises a BCC metallic solid solution and a boride phase. Interfacial segregation of boron atoms generates gradient-ordering phase boundaries (GOPBs), enhancing stress transfer and plastic compatibility. Strong interfacial bonding of GOPBs and the inherent stability of the dual-phase structure further enable remarkable resistance to ultrahigh-temperature softening. At 2073 K, GOPBs evolve into fully coherent interfaces, ensuring exceptional thermal stability at ~0.7 T_m . This work demonstrates a gradient-ordering strategy for achieving strength-plasticity synergy from ambient to ultrahigh temperatures.

Hypersonic vehicles with flight speeds above Mach 5 enable ultrafast transcontinental flights and rapid space access, showing great potential in space exploration, aerospace transportation, and military defense¹. Next-generation hypersonic vehicles, aiming at much higher Mach numbers and more reliable reusability, rely on aerothermal heating for hypersonic flight, enduring harsh service conditions under the coupling impacts of large heat fluxes and severe vibration². These extreme environments require vehicle materials capable of withstanding dramatic thermal gradients (from ambient to ultrahigh temperatures) and huge stagnation pressures (up to tens of megapascals). Therefore,

advanced materials with excellent high-temperature strength and thermal stability are critical for hot-end structures in hypersonic applications, such as engine combustors, nose tips, and leading edges^{3,4}. In the past decades, Nb-based, Mo-based, and W-based alloys have been widely used as hot-end structure materials due to their high melting temperatures (T_m) and excellent mechanical properties^{1,5}. However, they often suffer from element diffusion-controlled coarsening or phase dissolution-induced softening at 0.56–0.7 T_m ⁵, limiting their service temperatures below 1800 K. Refractory high-/medium-entropy alloys (RH/MEAs) with single body-centered cubic (BCC) structure have

¹School of Materials Science and Engineering, Jiangsu Key Laboratory for Advanced Metallic Materials, Southeast University, Nanjing, China. ²Ministry of Education Key Laboratory of Structure and Thermal Protection for High-Speed Aircraft, Southeast University, Nanjing, China. ³School of Science, Harbin Institute of Technology, Shenzhen, China. ⁴Herbert Gleiter Institute of Nanoscience, School of Materials Science and Engineering, Nanjing University of Science and Technology, Nanjing, China. ⁵Defense Innovation Institute, Academy of Military Science, Beijing, China. ⁶These authors contributed equally: Bo Sun, Bingjie Wang. ✉ e-mail: qwang678@seu.edu.cn; liangxb_d@163.com; blshen@seu.edu.cn

emerged as promising candidates for ultrahigh-temperature environments, due to their remarkable softening resistance and outstanding thermal stability^{6–8}. The well-established NbMoTaW and NbMoTaWV alloys exhibit superior compressive yield strengths of 405 and 479 MPa at 1873 K, respectively, but suffer from severe embrittlement at ambient temperature^{9–11}. Efforts to enhance their room-temperature plasticity through alloying with metallic elements (e.g., Ti, Zr, Re) can lead to a compensatory reduction in high-temperature yield strength^{12–14}. The entrenched strength-plasticity trade-off with severe temperature dependence hinders further improvement in the yield strength at temperatures above 1873 K. Thus, there remains a critical demand to achieve excellent strength-plasticity synergy from ambient to ultrahigh temperatures, which helps promote the practical application of RH/MEAs at extreme temperatures.

A potential approach for improving the room-temperature plasticity without sacrificing the softening resistance is introducing non-metallic elements (e.g., C, N, Si) into RH/MEAs to construct a BCC-ceramic heterostructure^{15–19}. For instance, compared to the NbMoTaW RHEA, a dual-phase $\text{Re}_{0.5}\text{MoNbW}(\text{TaC})_{0.5}$ alloy comprising BCC solid solution and carbide exhibited an increased yield strength from 500 to 900 MPa at 1473 K, owing to the synergistic effects of hard and soft lamellar structure³. Nonetheless, the ceramic-reinforcement approach also presents several inherent limitations. One drawback is that the high fraction and large size of ceramic phases increase the cracking sensitivity, resulting in room-temperature embrittlement^{16,20,21}. Besides, the in-situ formed ceramic phases with complex composition are usually metastable at ultrahigh temperatures, leading to unavoidable phase transformation or structural coarsening as temperature rises to $-0.6T_m$, which impairs the ultrahigh-temperature applications^{22,23}. Therefore, refining ceramic phases and simultaneously enhancing their thermal stability is crucial for achieving superior mechanical performance across a wide temperature range. It was found that the boron addition-induced preferential segregation at interfaces provides multiple benefits, including improved room-temperature plasticity by mitigating oxide accumulation at grain boundaries²⁴ (GBs), reinforced high-temperature performance by strengthening phase boundary (PB) cohesion²⁵, and enhanced thermal stability by modifying interfacial ordering^{26,27}. These findings highlight the significance of addressing interfacial issues, such as strain incompatibility and weak bonding, to simultaneously improve ambient plasticity, high-temperature strength, and thermal stability. However, the influence of interface modification on the mechanical performance of ceramic-reinforced RH/MEAs toward ultrahigh-temperature applications has been rarely investigated. Moreover, introducing B to the in-situ form ceramic phase is generally deemed ineffective for improving the strength above 1473 K, as borides exhibit lower melting temperatures compared to carbides or nitrides. These dilemmas underscore the necessity of developing novel ceramic-reinforced RH/MEAs with excellent ultrahigh-temperature performance and considerable room-temperature plasticity, which remain significant challenges.

Here, our work presents a dual-phase $(\text{W}\text{TaV})_{90}\text{B}_{10}$ RMEA comprising a BCC metallic solid solution and a boride ceramic phase. This RMEA yields an excellent strength-plasticity synergy from ambient temperature to ultrahigh temperature of 2073 K and concurrently achieves remarkable thermal stability up to $-0.7T_m$. The integration of a ceramic-reinforced heterostructure with boron segregation-induced interfacial ordering fosters the development of gradient-ordering phase boundaries (GOPBs). The semi-coherent GOPBs operate as a strain mediator and enable dislocations to slide from the soft solid solution to the hard boride, not only effectively alleviating stress concentration at interfaces, but also improving the ability to strain accommodation. Moreover, the ordered B-rich clusters at GOPBs strengthen the interfacial cohesion, thereby overcoming the strength-plasticity trade-off across a wide temperature range, where inherent in previously developed ceramic-reinforced RHEAs.

Results

Microstructure evolution and mechanical properties

The microstructural evolution of as-cast $(\text{W}\text{TaV})_{100-x}\text{B}_x$ ($x = 0, 5, 10, 15$, and 20 at.%) RMEAs with varying B contents (denoted as B_0 , B_5 , B_{10} , B_{15} , and B_{20}) was systematically investigated using X-ray diffraction (XRD), scanning electron microscope (SEM), and electron back-scattering diffraction (EBSD) analyses (Supplementary Figs. 1 and 2). The B_0 RMEA exhibits a single BCC structure, and the addition of B induced the formation of a boride phase, accompanied by a remarkable decrease in the intensity of the BCC diffraction peaks. The SEM and EBSD results are consistent with the XRD patterns. The B_0 RMEA exhibits a dendrite morphology, and the dendritic and interdendrite regions are both confirmed as the BCC phase by EBSD analysis. The B_5 RMEA shows a dual-phase microstructure with the interdendrite region transforming into a boride phase. As the B content increases to 10 at.%, the interdendrite boride phase forms interwoven BCC-boride lamella plates. Higher B content (B_{15}) leads to more lamellar precipitation. Further addition of B inhibits the formation of large BCC dendrites, which significantly refines the microstructure of B_{20} RMEA. As shown in Supplementary Fig. 3a, the variation in the volume fractions of BCC and boride phases for B_x RMEAs was derived from the EBSD results. These results reveal the phase competition between the BCC and boride phases with increasing B content, which restrains the grain coarsening, particularly in the BCC phase (Supplementary Fig. 3b). Despite the high boride content, the BCC phase remains dominant in the B_{20} RMEA (Supplementary Table 1).

The compressive engineering stress-strain curves of B_x RMEAs at ambient temperature are presented in Fig. 1a. The yield strength increases significantly from 1330 to 3010 MPa as the B content rises from 0 to 20 at.% (Supplementary Table 2). However, the increase in yield strength is accompanied by a continuous decrease in plastic strain. The B_{10} RMEA achieves an excellent balance, exhibiting a high yield strength of 2160 MPa and a substantial plastic strain of ~6%. The B_{10} RMEA exhibits nearly double the strength of the B_0 alloy, with a modest reduction in plasticity, demonstrating a strength-plasticity synergy at room temperature (Supplementary Note 1 and Supplementary Fig. 4). Besides, the B_{10} RMEA also exhibits excellent resistance to softening at elevated temperatures. It maintains a high yield strength of 1125 MPa at 1473 K and 650 MPa at 1873 K, as shown in Fig. 1b and Supplementary Table 3. Notably, it retains a yield strength of 242 MPa at 2073 K. Furthermore, it also presents excellent ultimate strength with values of 1790, 790, and 436 MPa at 1473, 1873, and 2073 K, respectively, without fracture at strains up to 30%. Comparative analyses reveal that the B_{10} RMEA presents not only superior yield strength but also excellent resistance to softening across a wide temperature than the existing RH/MEAs^{9,28–30}, RHEAs doping with non-metallic elements²⁴ (C, B), RHEAs reinforced with ceramic phases^{16,31,32}, refractory alloys³³ (RAs), and carbide-reinforced RAs³⁴ (Fig. 1c–e, Supplementary Figs. 4–7, Supplementary Table 4, and Supplementary Note 1). Specifically, Fig. 1d highlights the enhancement provided by the boride phase to the B_{10} RMEA, considering that the melting points of carbide and nitride ceramic phases are generally much higher than those of borides. Yielding with superior strength at similar homologous temperatures (T/T_m , where T_m was estimated using the rule-of-mixture method³⁵ and verified by experiments in Supplementary Note 2, Supplementary Figs. 8, 9, Supplementary Movies 1, 2, and Supplementary Table 5), the B_{10} RMEA demonstrates a higher operating temperature and enhanced safety than other materials. Given the importance of density in aerospace structural applications, the B_{10} RMEA also exhibits an excellent combination of specific yield strength at 1873 K and plastic strain at ambient temperature (Fig. 1e). Notably, B_{10} RMEA shows negligible size effect on the yield strength and plastic strain over a wide temperature range (Supplementary Fig. 10 and Supplementary Note 1). Although room-temperature ductility is still challenging for B_{10} RMEA (Supplementary Fig. 11), the compressive

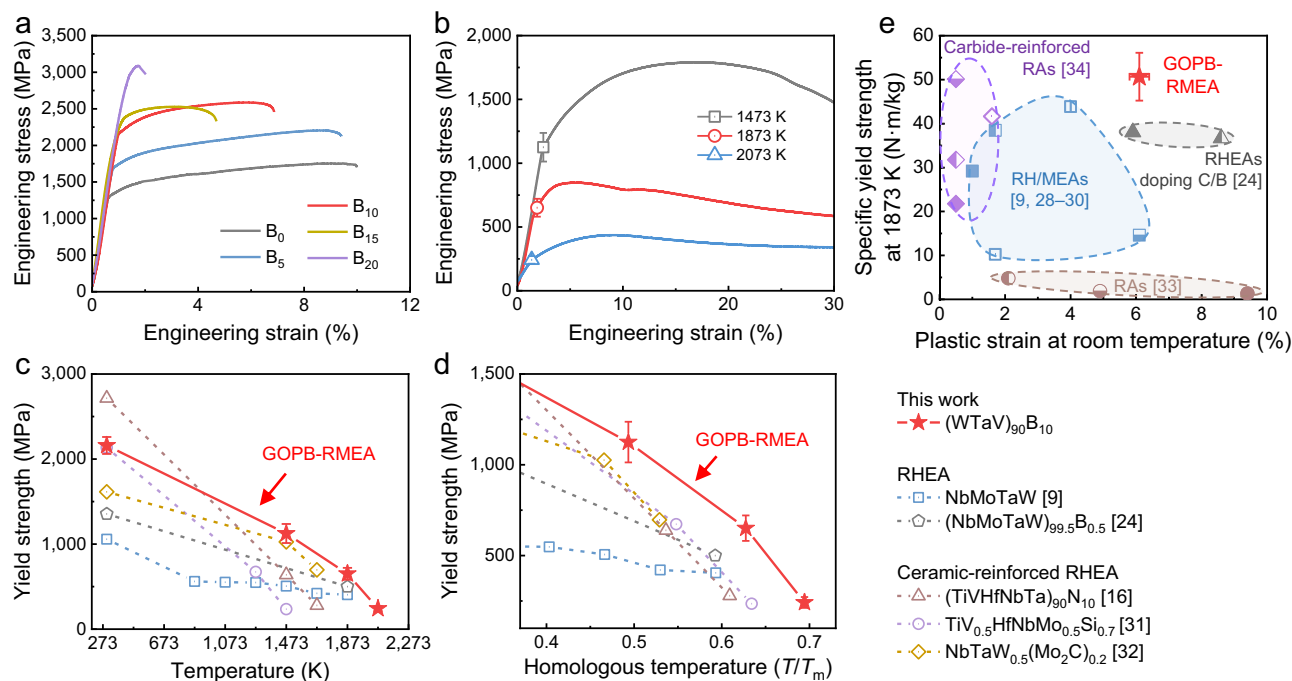


Fig. 1 | Mechanical properties of the B_x RMEAs. Stress–strain curves at **a** 298 K and **b** elevated temperatures. Yield strength evolution along with the increasing **c** test temperature (T) and **d** homologous temperature (T/T_m), with the melting temperature T_m estimated using the rule-of-mixture method). **e** Specific yield strength at 1873 K versus room-temperature plasticity. In image **e**, GOPB-RMEA, RH/MEAs, RHEAs doping C/B, RAs, and carbide-reinforced RAs represent refractory medium-entropy alloy with gradient-ordering phase boundary ((WTaV)₉₀B₁₀ in this

work), refractory high-/medium-entropy alloys, refractory high-entropy alloys doping with C/B elements, refractory alloys, and carbide-reinforced refractory alloys, respectively, which have published the mechanical properties at both room temperature and 1873 K. Detailed information on the mechanical properties in image **c–e** is listed in Supplementary Table 4. Error bars in **b–e** represent the standard deviation derived from three independent experiments. Source data are provided as a Source Data file.

strength–plasticity trade-off from ambient to ultrahigh temperatures has been effectively overcome.

Gradient-ordering phase boundaries

The microstructure of the interdendrite region of B₁₀ RMEA was analyzed by the dark-field transmission electron microscope (TEM), showing the alternating BCC and boride morphology (Fig. 2a). Selected area electron diffraction (SAED) analysis reveals that the BCC phase is a chemical-disordered solid solution, while the boride is an M₃B₂ (M = Ta, V, W) type tetragonal phase (Fig. 2b, c). The high-resolution TEM (HRTEM) image in Fig. 2d shows a semi-coherent PB with a calculated lattice mismatch of 0.08 between the M₃B₂ and BCC phases. Fast Fourier transformation (FFT) images of the yellow and blue areas (Fig. 2e, f) further confirm the presence of the M₃B₂ and BCC phases. Moreover, a distinctive ordered structure, as indicated by its (100) superlattice spots in the FFT image (Fig. 2g), with severe lattice distortion (Fig. 2h), is observed at the phase interface. In contrast, no superlattice diffraction is observed in the B₀ RMEA (Supplementary Fig. 12), suggesting that the ordered structure originates from the boride phase. The as-cast microstructure of B₁₅ and B₂₀ RMEAs was also analyzed by TEM (Supplementary Figs. 13 and 14), exhibiting a combination of BCC solid solution and MB (M = Ta, V, W) boride phase. The FFT and inverse FFT (IFFT) analyses indicate the formation of a conventional semi-coherent PB without additional superlattice diffraction or severe lattice distortion in B₁₅ and B₂₀ RMEAs. These observations preliminarily suggest that the excellent mechanical properties of the B₁₀ RMEA are likely attributed to the unique ordered structure at the BCC-M₃B₂ PBs. To further investigate the configuration of the ordered structure, the atomic-scale elemental distribution at the PB in the B₁₀ RMEA was analyzed by the atom probe tomography (APT) technique. The three-dimensional reconstructed maps in Fig. 2i show a relatively uniform distribution of metallic elements on the BCC side of

PB. Figure 2j presents the composition profile along with the red arrow in Fig. 2i, revealing a high concentration of B with a slight increase of V near the PB, while W and Ta are uniformly distributed. The three-dimensional reconstruction with a 0.09/nm³–B iso-surface threshold in Fig. 2k clarifies that the B-rich clusters appear near the PB, while almost no cluster is observed within the BCC phase. These observations and analyses unravel the origin of the ordered structure in Fig. 2g from B-rich clusters, which aligns with the capability of B atoms to preferentially segregate at the interface and modulate the interfacial ordering^{26,27}. The elemental reconstruction on the M₃B₂ phase side of PB exhibits a uniform distribution of B atoms (Fig. 2l, m). Besides, compared to the fully random configuration, a more localized distribution of B atoms is found in the M₃B₂ phase (Supplementary Fig. 15), which evidences the ordered configuration³⁶. These characteristics indicate that the M₃B₂ boride may adopt a V₃B₂-type D_{5a} structure with specific atomic occupation sites for B atoms (4g, Wyckoff position^{37,38}). Based on the above analyses, the B segregation-originated GOPB is observed, involving ordered B in the M₃B₂ boride phase, ordered B clusters around the PB, and disordered interstitial B atoms within the BCC phase, as illustrated by the schematic diagram in Fig. 2n. Moreover, the volume fraction of GOPBs is estimated as 0.14–0.35% within a layer of 2–5 nm near the PBs (Supplementary Fig. 16 and Supplementary Note 3).

Deformation behaviors at ambient and ultrahigh temperatures

Fracture surface and cross-sectional morphology of the B_x RMEAs after room-temperature compression were analyzed by SEM (Supplementary Figs. 17 and 18). All B_x RMEAs exhibit transgranular fracture, characterized by arrays of cleavage steps and various river patterns, and cracks preferentially initiate in the boride phase at the interdendrite region, indicating that the boride phase cannot improve intrinsic plasticization. The contribution of the boride

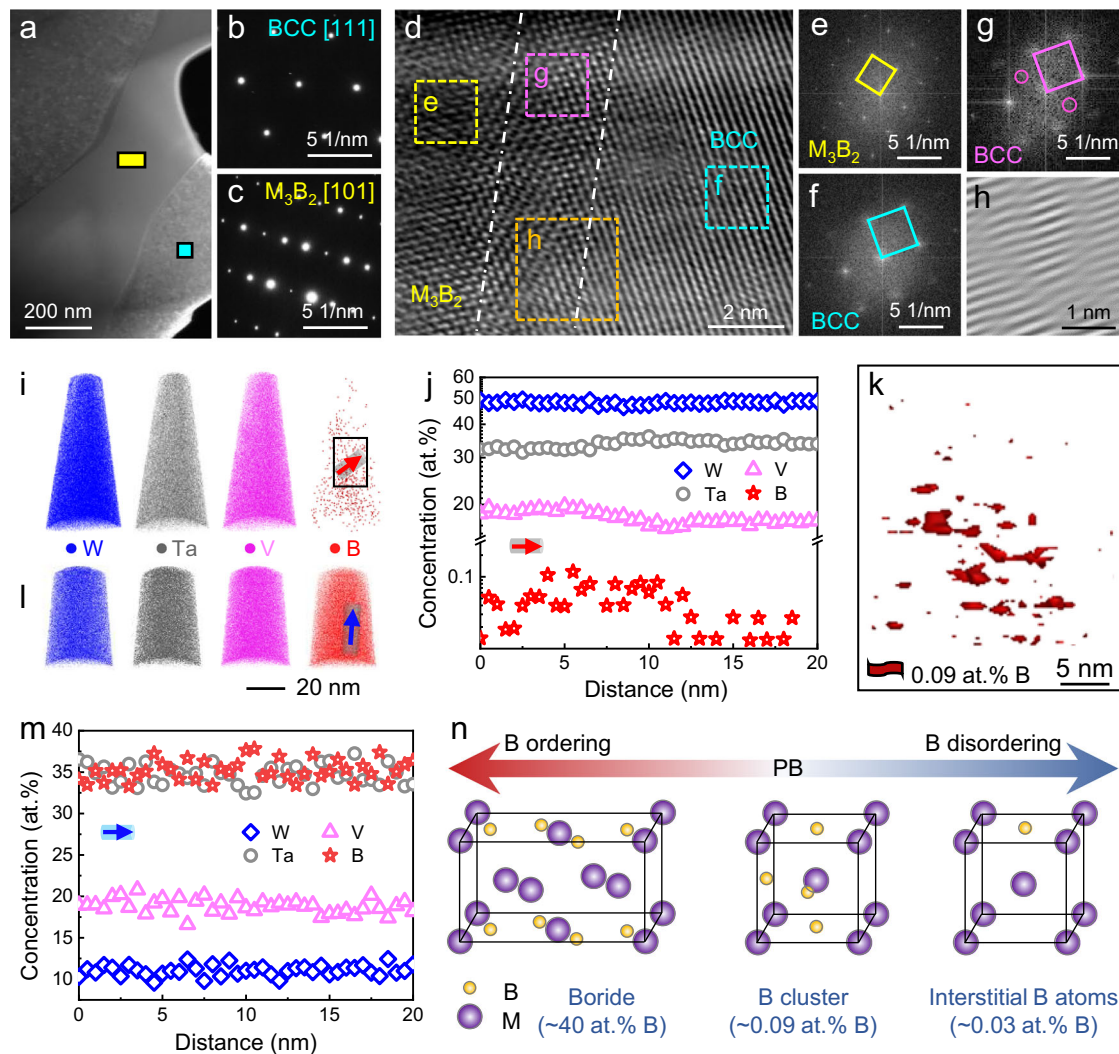


Fig. 2 | Microstructure of B_{10} RMEA. **a–c** Dark-field image and the SAED patterns show a dual-phase structure of BCC solid solution and M_3B_2 ceramic boride in B_{10} RMEA. **d–h** HRTEM image and the corresponding FFT and IFFT images indicate an ordered structure near the PBs. The magenta circles in image **g** indicate superlattice spots. Three-dimensional APT analysis reveals **i–k** the B-rich clusters near the PB in the BCC phase, and **l** and **m** the uniform distribution of elements in M_3B_2 boride.

n Schematic diagram of the GOPB, including ordered B occupation in boride, ordered B clusters near the PB, and completely disordered interstitial B atoms inside the BCC phase. The yellow and purple balls represent boron atoms and randomly distributed metal atoms (W, Ta, and V), respectively. Source data are provided as a Source Data file.

phase to the mechanical properties of B_x RMEAs can be considered in two aspects: (i) dual-phase heterogeneity and (ii) gradient-ordering configuration of the PBs. For the first aspect, the effect of the M_3B_2 phase on the mechanical properties is primarily driven by dual-phase heterogeneity. The hardness of M_3B_2 is approximately three times higher than that of the BCC phase (Supplementary Fig. 19a, b). This pronounced heterogeneity indicates that the boride phase requires significantly higher stress to activate dislocation slip for plastic deformation¹⁶, whereas only smaller stress is needed for a similar process in the BCC phase, as evidenced by the earlier pop-in behavior observed in the BCC phase (Supplementary Fig. 19c). During deformation, the hard M_3B_2 phase can generate back stress and constrain the plastic flow in the softer BCC phase, contributing to high yield strength and substantial plasticity by preventing strain incompatibility^{39,40}. The cumulative distribution of nanoindentation hardness (H) for the B_x RMEAs further demonstrates the enhanced heterogeneity by increasing boride fraction (Supplementary Fig. 19d). However, alloying 20 at.% B leads to both an increased boride fraction and size, which impairs cracking tolerance, resulting in rapid fracture for the B_{20} RMEA.

For the second aspect, the contribution of GOPBs during plastic deformation depends on their influence on crack propagation behavior. While massive short cracks are observed in B_{10} RMEA, many of them are blunted by the GOPBs. Besides, fine and dense BCC-boride lamellar at the interdendrite can promote crack deflection, thereby suppressing the rapid propagation of cracks. Although cracks can also be deflected by the fine lamellar and blunted by PBs in B_{15} RMEA, some of them cleave the BCC dendrites or propagate along the PBs. Given the higher ultimate compressive strength of B_{10} RMEA than B_{15} RMEA (Fig. 1a), GOPBs are crucial for enhancing interfacial bonding strength in B_{10} RMEA. This strong bonding inhibits the cleavage of BCC dendrites and impedes crack propagation along PBs, thus suppressing rapid fracture during plastic deformation. Consequently, the decent plasticity of B_{10} RMEA originates from: (i) the high-fraction BCC phase primarily accommodates plastic deformation; (ii) fine BCC-boride lamellar at the interdendrite region improves plasticity by deflecting cracks; and (iii) GOPBs restrain cleavage cracking in BCC dendrites and mitigate rapid fracture along PBs.

It is widely accepted that the ordered structure not only serves as a strong short-range obstacle to dislocations for increasing strength,

but also promotes dislocation coplanar slip for enhancing plasticity³. To understand the specific contribution of GOPBs in plastic deformation at room temperature, we characterized the dislocation configuration and local stress distribution in the pre-strained B₁₀ RMEA (Fig. 3). In the B₁₀ alloy with 2% strain, dislocations are observed within the BCC phase, the M₃B₂ phase, and around the GOPBs (Fig. 3a–c), indicating the synergistic deformation of the boride phase and the BCC matrix. The activation of multiple slip systems in the BCC phase facilitates the intersection and entanglement of dislocations, thus promoting dislocation cross-slip and forest strengthening, which is crucial for enhancing the strain-hardening effect. Specifically, both interstitial B-induced chemical fluctuations and B-ordered clusters serve as pinning points for dislocation sliding^{41–43}. When strained to 6%, pronounced dislocation entanglements are observed both within the BCC phase and around the GOPBs in the B₁₀ RMEA (Fig. 3d–f). Notably, the GOPBs not only contribute to the intersection and multiplication of dislocations within the BCC phase but also facilitate dislocations sliding into the M₃B₂ phase. This demonstrates the mediator role of GOPBs in stress transfer, which promotes compatible deformation. EBSD results reveal that the B₁₀ specimen with 6% deformation is composed of BCC and M₃B₂ phases with essentially unchanged volume fraction (Supplementary Fig. 20a). Kernel average misorientation (KAM) analysis presents a higher dislocation density in the BCC phase compared to the M₃B₂ phase (Supplementary Fig. 20b, c). The larger KAM values in the BCC matrix suggest that the relatively softer BCC phase

contributes more to plastic deformation. Specifically, the accumulation of geometrically necessary dislocations (GNDs) around the PBs leads to the formation of a cellular-distributed misorientation within the BCC dendrites (Fig. 3g, h). This indicates that the GOPBs can accommodate more concentrated GNDs to facilitate strain compatibility, thus enhancing the plasticity of the alloy. Severe lattice distortion is found around the GOPBs by geometric phase analysis⁴⁴, while moderate and slight lattice distortions are observed within the BCC and M₃B₂ phases, respectively (Fig. 3i–l). These findings further confirm the significant role of GOPBs in the plastic deformation of the B₁₀ RMEA.

After compression at 1873 and 2073 K, the B₁₀ RMEA remains its dual-phase structure, comprising a BCC solid solution and the M₃B₂ boride phase (Supplementary Fig. 21a, b). The minimal variations in phase fraction indicate that no significant phase transformations occurred under these ultrahigh-temperature compression tests (Supplementary Fig. 21c), confirming the excellent phase stability of the B₁₀ RMEA. Moreover, we observed extremely sluggish coarsening after ultrahigh-temperature compression, as shown in Supplementary Fig. 21d. Compared to the as-cast sample, the B₁₀ RMEA deformed at 2073 K retains a uniform size distribution with negligible coarsening, demonstrating excellent thermal stability. In contrast, the previously reported RH/MEAs and ceramic-reinforced RH/MEAs typically underwent phase transformations, rapid structural coarsening, or recrystallization during compression at elevated temperatures^{21,22,45}.

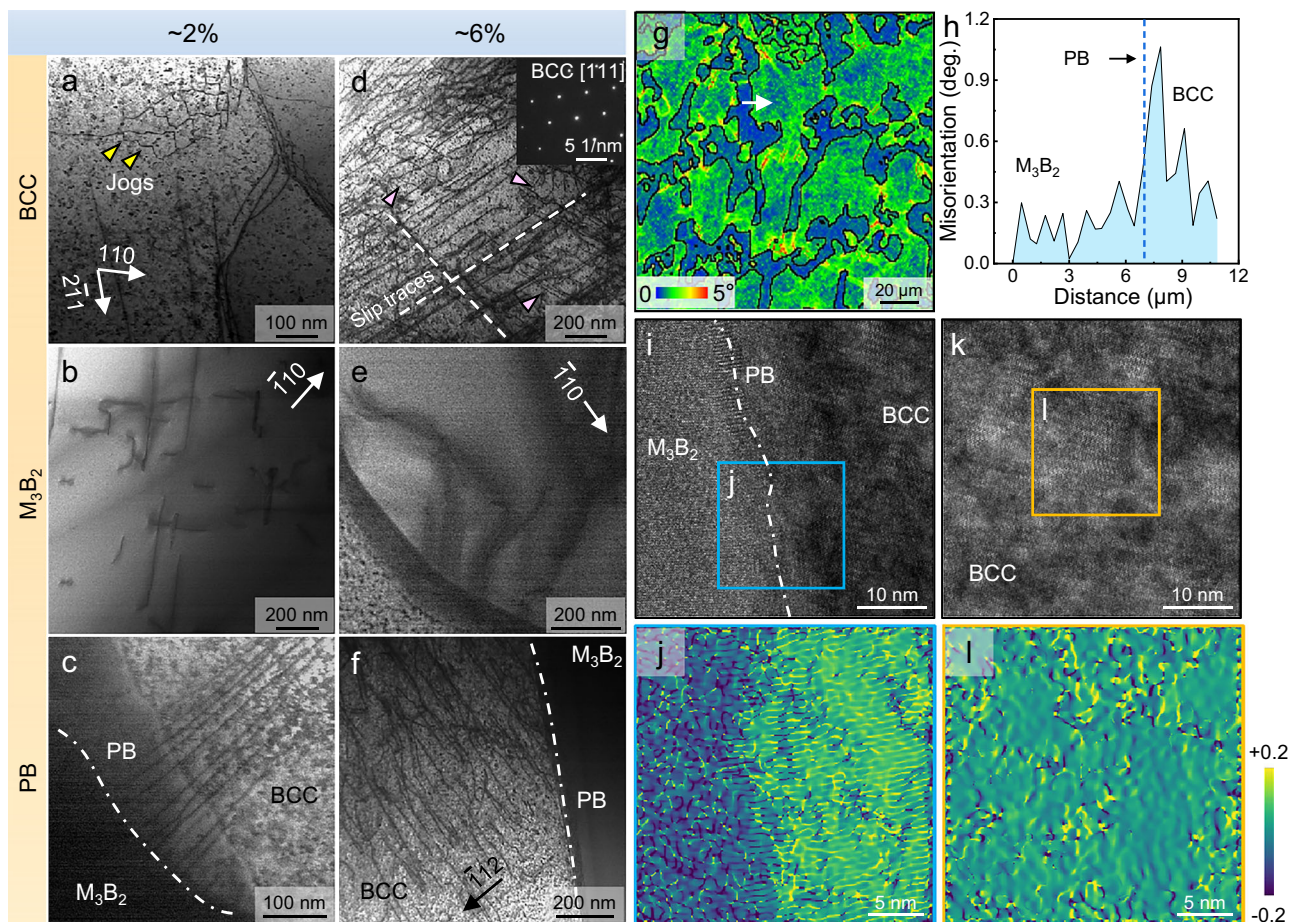


Fig. 3 | GOPB-mediated plasticity in B₁₀ RMEA at ambient temperature. Dislocation configurations as strained of **a–c** 2% and **d–f** 6%. The yellow triangles in image **a** indicate the jogs that are left by cross-slip dislocations. The inset in image **d** shows the SAED pattern of the BCC phase, and the pink triangles point out different planar dislocations. **g** KAM map and **h** misorientation distribution along

the white arrow in image **g** reveal the accumulation of high-density GNDs at GOPBs. HRTEM image with corresponding lattice strain distribution **i** and **j** at the GOPB and **k** and **l** within the BCC phase in the 6% strained specimen. Source data are provided as a Source Data file.

However, the B_{10} RMEA exhibits exceptional resistance to thermally driven softening and coarsening, even at temperatures approaching $-0.7T_m$. This remarkable thermal stability suggests that the B_{10} RMEA is particularly suitable for ultrahigh-temperature applications. Further EBSD and TEM analyses provide insights into the underlying mechanisms for the ultrahigh-temperature softening resistance of the B_{10} RMEA. Planar dislocations are observed in both the BCC and boride phases in the B_{10} RMEA compressed at 1873 K (Supplementary Fig. 22a–d). Particularly, a few dislocations are mediated across the GOPBs from the BCC phase to the M_3B_2 phase, resembling the mechanism of borrowed dislocations⁴⁶. Besides, the element distribution map in Supplementary Fig. 22e reveals the formation of V-rich PB after compression at 1873 K, which is likely responsible for the occurrence of PB-mediated dislocations. At 2073 K, additional activated slip systems facilitate the dislocation entanglement in the BCC phase, which enables a strong dynamic Hall–Petch effect (Fig. 4a)

to resist rapid softening during the latter stages of deformation⁴⁷. Arrays of planar dislocations intersect, forming immovable jogs and multiplicative dislocation loops (Fig. 4b and c). This cross-slip behavior can be promoted by interstitial B atoms⁴⁸, which significantly contributes to the high dislocation density in the BCC phase. Planar dislocations are also found in the M_3B_2 phase (Fig. 4d), and ~47% of them are identified as edge dislocations by $g \cdot b$ analysis. This indicates that the boride phase possesses a certain degree of plastic deformation capability at 2073 K without undergoing excessive softening that could affect structural stability^{49,50}. Dislocation cross-slip is also observed at the PBs (Fig. 4e). EDS and HRTEM analyses reveal the V–B enrichment at the PBs, transforming the interface from semi-coherent to fully coherent after deformation at 2073 K (Fig. 4f–i). The negligible lattice mismatch inhibits the long-range diffusion of atoms across PBs, thus preventing phase transformation and the associated structural coarsening.

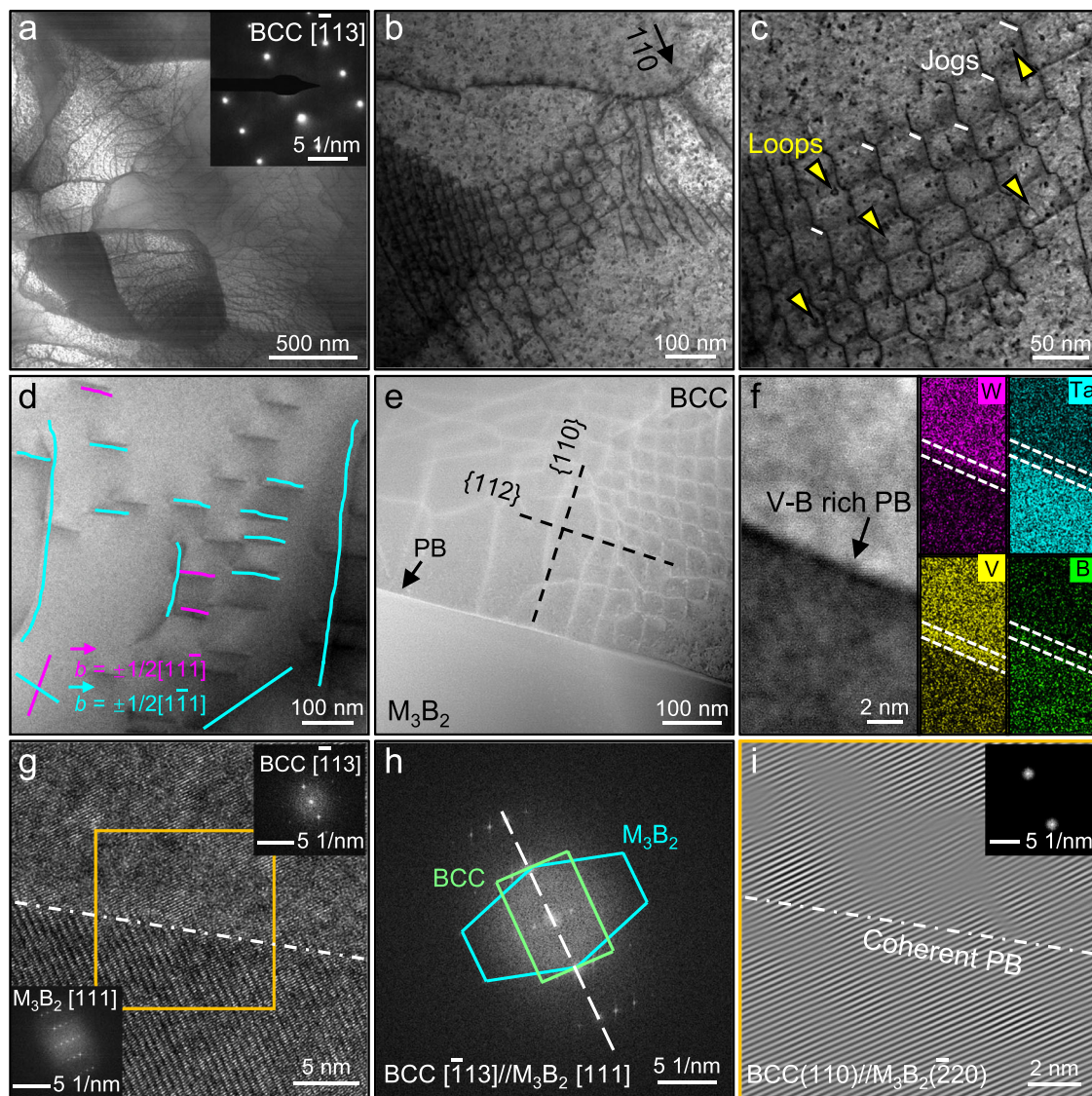


Fig. 4 | Microstructure evolution of B_{10} RMEA after deformation at 2073 K. a–c Dynamic Hall–Petch effect and forest dislocation strengthening in the BCC phase. The inset in image a shows the EBSD pattern of the BCC phase. White lines and yellow triangles in image c indicate jogs and loops, respectively. d Both screw and edge dislocations exist in the M_3B_2 phase. e and f Dislocation cross-slip near the V–B rich PB. g–i V–B segregation induces the transformation of PBs from semi-coherent

to fully-coherent. The upper-right and lower-left insets in image g show the FFT patterns for the BCC and M_3B_2 phases, respectively. Image h is an FFT image corresponding to image g. Image i is the IFFT image from the orange square in image g, where the inset shows the corresponding FFT image for the parallel orientation BCC(110)// M_3B_2 ($\bar{2}20$). Source data are provided as a Source Data file.

Long-term thermal stability of gradient-ordering phase boundaries

Annealing experiments were performed on B₁₀ RMEA at 1873 and 2073 K for 5 h to reveal the long-term thermal stability of GOPBs. The annealing treatments induce negligible change in phase composition, fraction, and size of dual phases, and room-temperature yield strength with plastic strain as compared to the as-cast alloy (Supplementary Fig. 23), demonstrating excellent thermal stability of B₁₀ RMEA after long-term annealing up to $-0.7T_m$ (2073 K). Further TEM analyses confirm the persistence of the BCC-M₃B₂ dual-phase architecture after annealing at 1873 and 2073 K (Supplementary Fig. 24). Besides, both the HAADF images and element mappings reveal a V-segregated PBs with a width of 2–3 nm, which is analogous with the PBs after compression at 1873 and 2073 K (Fig. 4f and Supplementary Fig. 22e). Crucially, the superlattice spots indicative of the interfacial ordered structure are also found around PBs but absent in regions distant from the interface (Supplementary Figs. 25, 26), directly verifying the thermal stability of GOPBs in B₁₀ RMEA up to 2073 K. Notably, the volume fraction of the ordered region decreases concurrently with the pronounced element segregation upon annealing. This evolution strongly suggests that the superlattice spots originate from chemical short-range ordering of B atoms (evidenced by B clusters in Fig. 2k) rather than their long-range periodic ordering occupation within the crystal lattice. Therefore, the thermal stability of GOPBs is independent of stress, heat, or their coupling effect (Supplementary Figs. 20, 21, 23), which certifies the advantage of the element-segregation-induced interfacial ordering strategy.

Discussion

The above results demonstrate that the B₁₀ RMEA exhibits an admirable combination of large room-temperature plasticity, superior ultrahigh-temperature strength, and exceptional phase and thermal stability up to $-0.7T_m$, which is attributed to the unique gradient-ordering structure. The formation of GOPBs in the B₁₀ RMEA can be primarily attributed to both thermodynamic and kinetic factors: (i) the segregation tendency of B at the PBs and (ii) the incomplete diffusion of B at the phase front during solidification. Previous studies have demonstrated that B addition significantly influences the interfacial ordering through B segregation^{26,27}. To investigate the segregation tendency of B, we examined the segregation energy (E_s) using density functional theory (DFT) calculations. For B₁₀ RMEA, the BCC phase was represented by W₄₈Ta₃₄V₁₈, and the tetragonal M₃B₂ boride phase was defined according to its composition and crystal structure (P4/mbm, $a = b = 6.184 \text{ \AA}$, $c = 3.284 \text{ \AA}$, $\alpha = \beta = \gamma = 90^\circ$). The constructed atomic models were depicted in Fig. 5a–i, corresponding to the Supplementary Data 1–9, wherein the used elemental contents were provided in Supplementary Table 6. The segregation tendency of B at the PB was investigated by calculating the segregation energy E_s as follows^{51–53}:

$$E_s = (E_{PB}^B - E_{PB}) - (E_{bulk}^B - E_{bulk}) \quad (1)$$

where E_{PB}^B and E_{PB} represent the total energies of the interface models with and without the B atoms at the PB, respectively. Similarly, E_{bulk}^B and E_{bulk} denote the total energies of the interface models with and without the B element within the BCC phase, respectively. Therefore, a negative E_s value indicates that the segregation of the B element toward the PB is energetically favored⁵⁴. As shown in Fig. 5j, the segregation energy E_s of the B element at the PB is negative and more negative than that at the GB of NbMoTaW alloy²⁴ (-4 eV), indicating a strong segregation tendency of B toward the PB. This leads to the formation of B-rich clusters between the BCC and M₃B₂ phases.

Detailed FFT analysis reveals no extra diffraction spots at the PB of the B₁₅ and B₂₀ RMEAs (Supplementary Figs. 13, 14), suggesting the absence of B-ordered clusters between the BCC and MB phases. This discrepancy possibly arises from that the B_x RMEAs have undergone

different solidification processes with the increase of B content (Supplementary Fig. 27). The equilibrium phase diagrams show that B₅ and B₁₀ RMEAs experienced a solid-state phase transformation (BCC + MB \rightarrow M₃B₂), whereas no additional phase transformation occurred after the disappearance of the liquid phase in B₁₅ and B₂₀ RMEAs. The formation of M₃B₂ requires a volume reduction of the BCC phase, which leads to the migration of PBs toward the interior of the BCC phase. Diffusion-mediated interface migration is insufficient at the front of the transformed phases during non-equilibrium solidification, thus leaving B-rich clusters near the PBs. Typically, it usually shows a strong orientation relationship when ceramic phases in-situ precipitate from the BCC solid solution. However, the B₂₀ RMEA exhibits a monotonic orientation relationship, whereas the B₁₀ RMEA shows a distribution of diverse orientation relationships (Supplementary Fig. 28). This diversity suggests that adjusting the B content to enable the alloy to undergo solid-state phase transformation during solidification can promote the formation of GOPBs. Notably, although arc melting typically induces non-equilibrium solidification under rapid cooling, solid-state phase transformation (BCC + MB \rightarrow M₃B₂) indeed occurs due to the undetectable MB phase in the as-cast B₁₀ RMEA (Fig. 2a) and sufficiently slow cooling rate at later-stage solidification (Supplementary Fig. 29). Furthermore, the completion of solid-state phase transformation was further evidenced by the stationary PBs during in-situ annealing and the unchanged microstructure after long-term annealing at ultrahigh temperatures (Supplementary Figs. 30, 23, and Supplementary Note 4).

Here, we quantitatively evaluate the significance of GOPBs to the yield strength (σ_y) of B₁₀ RMEA by calculating the individual contributions⁵⁵ from solid solution strengthening ($\sigma_0 + \sigma_{ss}$), grain boundary strengthening (σ_{gb}), precipitation strengthening (σ_p), dislocation strengthening (σ_d), and interstitial strengthening (σ_i). The PB-contributed strength ($\Delta\sigma_{PB}$) was defined as the difference between the yield strength and the summation of the strength from other individual contributions (Supplementary Note 5 and Supplementary Table 7). The calculation results reveal that the multi-principal composition ($\sigma_0 + \sigma_{ss}$) primarily determines the superior yield strength σ_y of B₁₀ RMEA at both ambient and elevated temperatures. Additionally, $\Delta\sigma_{PB}$ contributes $\sim 32\%$ to σ_y at ambient temperature and retains $\sim 23\%$ at 1873 K, highlighting the significance of PB strengthening in B₁₀ RMEA.

The strength contribution of GOPBs originates from their intrinsic bonding characteristics. To evaluate the effects of the B element on the binding strength between BCC and M₃B₂ phases, the binding energy (E_b) was calculated as follows⁵⁶:

$$E_b = (E_{PB}^B - E_{PB}) - (E_{FS}^B - E_{FS}) \quad (2)$$

where E_{FS}^B and E_{FS} represent the total energies of the fracture models with and without the B element at the PB, respectively. The value of E_b can be regarded as the energy penalty required for the PB to fracture into two free surfaces⁵⁷. The obtained negative E_b shown in Fig. 5k manifests that B segregation at the PB is conducive to PB strengthening. Moreover, the negative values of E_b are almost proportional to the B content at PB, indicating that the formation of B-enriched clusters can effectively improve the PB binding strength. Therefore, the favorable segregation of B at the PB promotes the formation of B-rich clusters, while the increased B content enhances the PB binding strength. To further understand the PB strengthening mechanism affected by B segregation, the B–B interaction at the PB (one B atom is located at the PB while another B atom belongs to the M₃B₂ phase) was investigated by analyzing the partial density of states (PDOS) and two-dimensional electron density difference (Fig. 5l, m). The PDOS analysis shows significant overlap of the *s* and *p* electronic orbitals for both B atoms, indicating a strong bonding interaction. Besides, the two-dimensional electron density difference reveals a strong interaction between the two B atoms at the PB and the boride, as shown by the

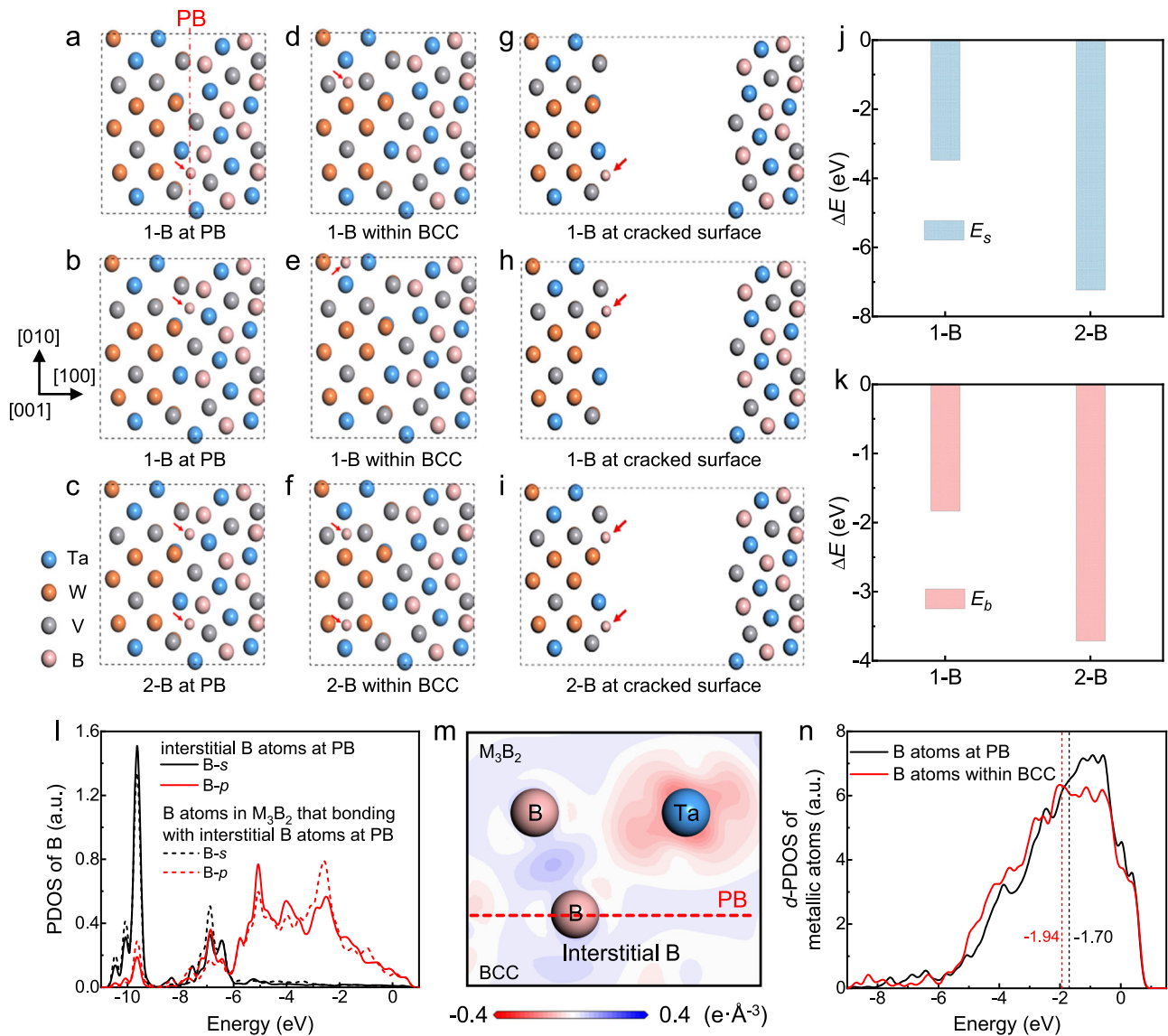


Fig. 5 | Contribution of the GOPBs in B_{10} RMEA. **a–i** Atomistic configurations with the orientation relationship of $(200)_{BCC} W_{48}Ta_{34}V_{18}/(001)_{Tetragonal} M_3B_2$. **a–c** illustrates the interface models with **a** and **b** one interstitial B atom (1-B) and **c** two interstitial B atoms (2-B) located at PB. **d–f** illustrates the interface models with **d** and **e** 1-B and **f** 2-B within the BCC phase. **g–i** illustrates the PB-cracked interface models with **g** and **h** 1-B and **i** 2-B located at the BCC surface. The interstitial B atoms with a small diameter are highlighted by the red arrows. **j** Segregation energy (E_s) and **k** binding energies (E_b) obtained from a series of atomistic models with 1-B and 2-B at PB. **l** PDOS of the interstitial B atoms at PB and the B atoms in Ta_3B_2 , which are bonding with the interstitial B atoms at PB. The energy of zero indicates the Fermi

level (E_F). **m** Two-dimensional electron density difference between the interstitial B atom at PB with the B and Ta atoms in Ta_3B_2 . Red and blue represent the depletion and accumulation of electrons, respectively, with the unit of $e \cdot \text{\AA}^{-3}$. **n** d -PDOS of the metal atoms when neighboring with the interstitial B atoms that are located at PB or within the BCC bulk. The energy of zero indicates the Fermi level (E_F). The black and red dotted lines highlight the positions of the d -band center of the metal neighbors when the interstitial B atom is located at PB and within the BCC bulk, respectively. Atomistic configurations for electronic structure calculations have been supplied as Supplementary Data 1–9. Source data are provided as a Source Data file.

charge accumulation area in Fig. 5n, confirming a covalent bonding characteristic. This special B–B covalent bonding may account for the improved PB binding strength due to B segregation. Moreover, Fig. 5n shows a more localized d -PDOS curve with the d -band center closer to the Fermi level (E_F) when the interstitial B atoms are situated at the PB, compared to their position within the BCC phase. This demonstrates a stronger metallic bonding between B with metal atoms as the B element segregates at the PB⁵¹, contributing to not only the interfacial bonding strength but also the plastic deformability. Consequently, both the covalent bonding characteristic of B–B and the enhanced interaction between the interstitial B element and adjacent metal atoms at the PB contribute to the enhanced PB binding strength due to B segregation.

In addition to their contribution to yield strength, GOPBs also play a key role in determining both the plastic deformation and thermal stability of B_{10} RMEA. For the decent ambient plasticity, the gradient ordering structure around the semi-coherent GOPBs can enhance the capability for dislocation storage, preventing interfacial stress concentration and promoting strain compatibility within the strong heterostructure. Specifically, the misorientation gradient is uniformly distributed around all PBs with a peak misorientation degree of -1° in B_{10} RMEA (Fig. 3g, h), while it concentrates around only a few PBs with a quite large peak misorientation degree up to -14° in B_{15} RMEA (Supplementary Fig. 20e, h). The uniform distribution of misorientation gradient and low degree of peak misorientation suggest that GOPBs can promote coordinated hetero-deformation between the

dual-phase architecture in B_{10} alloy. Conversely, the absence of GOPBs in B_{15} RMEA leads to localized stress concentration, which is consistent with the pronounced susceptibility to fracture along PBs (Supplementary Fig. 18). Consequently, GOPBs contribute significantly to room-temperature deformation by promoting coordinated deformation across dual phases and mitigating stress concentration to avoid early cracking. The second factor is the bonding characteristic that enables GOPBs to act as a mediator, facilitating the emission of dislocations from the soft BCC phase to the hard M_3B_2 phase. This mechanism, referred to as borrowed dislocations, can provide significant plasticity to the nano-/micro-scale ceramic phase⁴⁶. During deformation at ultrahigh temperatures, the GOPBs also contribute to the strong binding strength. The compressed B_{10} RMEA shows sparse and uniformly distributed micropores within the middle region (Supplementary Fig. 31a, b), while the bottom region is nearly pore-free (Supplementary Fig. 31c, d). In contrast, both the middle and bottom regions in the compressed B_{15} RMEA exhibit massive pores (Supplementary Fig. 31e–h). Notably, many of these pores form at PBs through the coalescence of micropores. This observation directly demonstrates that the weak bonding strength of conventional PBs in B_{15} RMEA is unfavorable for maintaining strength and impedes coordinated plastic deformation at ultrahigh temperatures. Furthermore, detailed TEM analyses reveal an absence of either element segregation or interfacial ordered structure around the PBs in compressed B_{15} RMEA (Supplementary Figs. 32, 33). This discrepancy further underscores that the superior ultrahigh-temperature performance of B_{10} RMEA, despite its lower boride fraction than B_{15} RMEA, stems from a structure advantage of GOPBs, i.e., the interfacial ordered structure induced by element segregation at PBs.

Regarding thermal stability, the advantage of GOPBs is mainly attributed to the suppression effect on diffusion-dominated interfacial migration⁵⁸ (Supplementary Note 6). The coarsening rate K^{59} is determined by the molar volume of the M_3B_2 phase (V_m^B) and the interfacial energy (γ). In other words, the phase coarsening rate depends on whether phase transformations occur or whether the characteristic of the PBs changes. In the as-cast B_{10} RMEA, the semi-coherent GOPBs present only a slight concentration of V and B at the ordered clusters (Fig. 2j). After compression at 2073 K, the PBs transform into fully coherent interfaces with significant enrichment of V and B (Fig. 4f–i). This transformation reduces lattice distortion and leads to a substantial decrease in interfacial energy (γ), strongly suppressing diffusion-controlled interfacial migration. As a result, both the fraction and size of the dual phases remain virtually unchanged after compression at 2073 K, demonstrating the excellent thermal stability of the B_{10} RMEA even at temperatures approaching $-0.7T_m$.

In summary, we developed a boride-reinforced (WTaV)₉₀B₁₀ RMEA with gradient-ordering phase boundaries, achieving a remarkable combination of decent ambient plasticity, considerable ultrahigh-temperature strength, and excellent thermal stability. B segregation at PBs during solid-state phase transformation fosters the formation of ordered B-rich clusters, where the covalent B–B bonding and the strong interaction between interstitial B atoms and their adjacent metal neighbors at the PB enhance interfacial cohesion. This nanoscale ordered structure at PB enables the B_{10} RMEA to exhibit substantial plasticity of ~6% at ambient temperature, alongside a high yield strength of 650 MPa at 1873 K and 242 MPa at 2073 K. The alloy maintains structural and phase stability after ultrahigh-temperature deformation, ensuring excellent thermal stability up to $-0.7T_m$. These findings demonstrate that the strength-plasticity trade-off from 298 to 2073 K is effectively overcome in our GOPB-reinforced RMEA. The interfacial gradient-ordering strategy offers a viable pathway for developing advanced RMEAs toward ultrahigh-temperature applications.

Methods

Alloy preparation and microstructure characterization

(WTaV)_{100-x}B_x alloys ($x = 0, 5, 10, 15, 20$ at.%, denoted as B₀, B₅, B₁₀, B₁₅, and B₂₀) were designed by introducing boron into the equiatomic WTaV alloy. The alloys were fabricated using a vacuum arc-melting furnace (Chengdu Zhongke Advanced Materials Technology Engineering Co., Ltd) under a high-purity argon atmosphere. Before melting the target ingots, a pure Ti ingot was melted for at least five minutes to absorb residual oxygen in the furnace. To ensure compositional homogeneity, each B_x ingot was melted for at least 3 min, then flipped and remelted more than five times. Melting was initiated at a current of 200 A, with subsequent remelting conducted at currents between 300 and 400 A. The ingots were finally furnace-cooled to room temperature within a water-cooled copper mold crucible. High-purity W, Ta, V, and B elements (details in Supplementary Table 8) were used as the raw materials. The initial weight of each pre-melted ingot was 20 g with a deviation of ± 0.005 g per element during the raw materials were weighed. Only ingots with a mass loss below 0.5 g after melting were retained for further analysis. The chemical composition of the ingots was confirmed by an inductively coupled plasma-optical emission spectrometer (ICP-OES, Agilent 5110). The ingots were mechanically crushed into powder with a particle size under 1 mm, and used as samples for ICP-OES tests after microwave digestion. The configurational mixing entropy was estimated using the equation⁶⁰ $\Delta S_{\text{mix}} = -R \sum_{i=1}^n c_i \ln c_i$, where R is the gas constant, n is the total number of constituent elements, and c_i is the molar fraction of the i th element. The calculated ΔS_{mix} values (Supplementary Table 9) confirm the B_x compositions as refractory medium-entropy alloys (B_x RMEAs). Long-term annealing was conducted on B_{10} RMEA ingots at 1873 and 2073 K, respectively, for 5 h by a high-vacuum tungsten-wire sintering furnace. The heating and cooling rates were both 10 K/min.

The crystalline structure and phase constitution of the B_x RMEAs were analyzed by X-ray diffraction (XRD, Bruker D8 Discover) with Cu-K α radiation at a scanning rate of 4°/min. The micromorphology was characterized using a field emission scanning electron microscope (SEM, FEI Nova Nano450). The phase structure was analyzed using an electron back-scattering diffraction (EBSD, FEI Sirion) with an accelerating voltage of 15–20 V and a specimen tilt of 70°. The binning mode of pixels, frame averaging, frame rate, and exposure time for EBSD tests were set as 4 × 4, 5, 64, and 2.16 ms, respectively. The quality statistics details of the EBSD data were provided in Supplementary Table 10. The SEM and EBSD specimens were prepared by a vibratory polisher (Buehler VibroMet 2) with a nanoscale SiO₂ suspension for 6 h. Phase maps, Kernel average misorientation (KAM) maps, and orientation relationship of the phase boundary were analyzed using Channel 5 software (version 5.0.9.0) after noise reduction by standard smoothing (zero solutions extrapolated no more than twice). Phase size was measured in the phase map by Nano Measurer software (version 1.2.5). The microstructure and element mappings of the as-cast and deformed specimens were characterized by a transmission electron microscope (TEM, Talos F200X) with an energy-dispersive X-ray spectroscopy (EDX). Fast Fourier transformation (FFT), inverse fast Fourier transformation (IFFT), and geometric phase analysis (GPA) were performed on the high-resolution TEM (HRTEM) images using Digital Micrograph software (version 3.7.4). All TEM samples were first mechanically ground to ~30 μm and then thinned by ion-milling (GATAN-M691). The chemical uniformity was evaluated by atom probe tomography (APT, CAMECA LEAP 4000X Si). Needle-shaped APT samples were fabricated by a focused ion beam (FIB, Zeiss Auriga). The APT samples were examined at 50 K under an ultrahigh vacuum of $\sim 4 \times 10^{-11}$ torr. Three-dimensional (3D) reconstructions of the APT data were performed using the Integrated Visualization and Analysis Software (IVAS 3.8.2).

Mechanical properties testing

Room-temperature compression tests were conducted using a Sans 5305 system, while the ultrahigh-temperature compression tests were performed in an argon atmosphere using a Zwick KAPPA 100 machine. An external infrared thermometer and a built-in thermocouple were calibrated against each other to ensure the test temperature accuracy within $\pm 6\text{ K}^{21}$. A strain rate of $1 \times 10^{-3}\text{ s}^{-1}$ was used at both ambient and elevated temperatures. The heating and cooling rates for ultrahigh-temperature compression tests were -50 and -20 K/min , respectively. Compression samples were cut using electrical discharge machining to dimensions of $\varnothing 2 \times 4\text{ mm}$ and $\varnothing 4 \times 8\text{ mm}$, followed by ultrasonically cleaning with alcohol. Nanoindentation tests were performed using a Hysitron Triboindenter (Hysitron Inc., Minneapolis, MN) at ambient temperature. Indentations were performed with a maximum load of 30 mN with a loading time of 10 s in load-controlled mode. A step interval of $10\text{ }\mu\text{m}$ was applied between successive indentations to prevent overlap of the deformed zones from adjacent indentations. Samples for nanoindentation tests were cut using electrical discharge machining to dimensions of $6 \times 6 \times 1\text{ mm}$, followed by mechanical grinding with sandpaper and vibrational polishing with a nanoscale SiO_2 suspension.

DFT computational details and phase diagram calculation methods

All the density functional theory (DFT) calculations were conducted based on the Cambridge Sequential Total Energy Package (CASTEP) module, which was implemented in Materials Studio 7.0⁶¹. The exchange and correction of atomic interactions were described by the generalized gradient approximation (GGA) method with Perdew–Burke–Ernzerhof (PBE) function⁶². The ultrasoft pseudo-potential method was adopted to describe the interactions between valence electrons and ionic cores⁶³. A plane-wave basis set was assigned with a cutoff energy of 400 eV . The Brillouin zone was sampled by a Monkhorst–Pack grid⁶⁴. The convergence tolerances of energy, force, and displacement for the structure optimization were $5.0 \times 10^{-6}\text{ eV/atom}$, 0.01 eV/\AA , and $5.0 \times 10^{-4}\text{ \AA}$, respectively, and the self-consistent field (SCF) was set as $5.0 \times 10^{-7}\text{ eV/atom}$.

A supercell model with a $(200)_{\text{BCC}}\text{W}_{48}\text{Ta}_{34}\text{V}_{18} // (001)_{\text{Tetragonal}}\text{M}_3\text{B}_2$ coherent interface and the k point of $(2 \times 2 \times 4)$ was constructed to investigate (i) the segregation tendency of B element toward PB and (ii) the binding strength of PB affected by interstitial B element. Note that the $\text{W}_{48}\text{Ta}_{34}\text{V}_{18}$ model represents the BCC phase in B_{10} , which was consistent with the composition measured in our 3D-APT experiments (Fig. 2 and Supplementary Table 6). The supercell model mentioned above was built based on the special quasi-random structure (SQS) method⁶⁵, which was generated using the Alloy Theoretic Automated Toolkit⁶⁶ (ATAT). Such a method was based on a Monte Carlo-based evolutionary algorithm to search for the periodic atomic structure with the closest match of correlation functions of an ideally mixed solid-solution state. The atomistic models are shown in Fig. 5a–i, with the atomistic configuration CIF files provided in Supplementary Data 1–9. Negative E_s indicated that the segregation of the B element toward PB was energetically favored. The negative binding energy indicated that the B element located at PB could enhance the phase interface bonding strength^{51,52,56}.

Phase diagram calculations of B_x RMEAs were performed using the Thermo-calc 2024b software with the TCHEA6 database^{67,68}. The equilibrium phase diagram and phase transformation stages were predicted based on the Gibbs energy minimization for a given composition of the B_x RMEAs.

Data availability

All data supporting the findings in this study are available within the main text, Supplementary Information, Supplementary Data files, and Source Data file. Source data are provided with this paper. The EBSD

and HRTEM raw data have been deposited on the Figshare database under the accession code <https://doi.org/10.6084/m9.figshare.30515822.v2>. Source data are provided with this paper.

References

- Peters, A. B. et al. Materials design for hypersonics. *Nat. Commun.* **15**, 3328 (2024).
- Prameela, S. E. et al. Materials for extreme environments. *Nat. Rev. Mater.* **8**, 81–88 (2023).
- Wei, Q. et al. Metal-carbide eutectics with multiprincipal elements make superrefractory alloys. *Sci. Adv.* **8**, eabo2068 (2022).
- Kuang, J. et al. Ablation-resistant yttrium-modified high-entropy refractory metal silicide $(\text{NbMoTaW})\text{Si}_2$ coating for oxidizing environments up to $2100\text{ }^\circ\text{C}$. *Mater. Today* **80**, 156–166 (2024).
- Tsakiropoulos, P. Alloys for application at ultra-high temperatures: Nb-silicide in situ composites; challenges, breakthroughs and opportunities. *Prog. Mater. Sci.* **123**, 100714 (2022).
- El Atwani, O. et al. A quinary WTaCrVHf nanocrystalline refractory high-entropy alloy withholding extreme irradiation environments. *Nat. Commun.* **14**, 2516 (2023).
- Senkov, O. N., Gorsse, S. & Miracle, D. B. High temperature strength of refractory complex concentrated alloys. *Acta Mater.* **175**, 394–405 (2019).
- Zou, Y., Ma, H. & Spolenak, R. Ultrastrong ductile and stable high-entropy alloys at small scales. *Nat. Commun.* **6**, 7748 (2015).
- Senkov, O. N., Wilks, G. B., Scott, J. M. & Miracle, D. B. Mechanical properties of $\text{Nb}_{25}\text{Mo}_{25}\text{Ta}_{25}\text{W}_{25}$ and $\text{V}_{20}\text{Nb}_{20}\text{Mo}_{20}\text{Ta}_{20}\text{W}_{20}$ refractory high entropy alloys. *Intermetallics* **19**, 698–706 (2011).
- Zou, Y., Maiti, S., Steurer, W. & Spolenak, R. Size-dependent plasticity in an $\text{Nb}_{25}\text{Mo}_{25}\text{Ta}_{25}\text{W}_{25}$ refractory high-entropy alloy. *Acta Mater.* **65**, 85–97 (2014).
- Kumar, P. et al. Degradation of the mechanical properties of NbMoTaW refractory high-entropy alloy in tension. *Acta Mater.* **279**, 120297 (2024).
- Li, T. et al. A novel ZrNbMoTaW refractory high-entropy alloy with in-situ forming heterogeneous structure. *Mater. Sci. Eng. A* **827**, 142061 (2021).
- Chanho Lee et al. Lattice distortion in a strong and ductile refractory high-entropy alloy. *Acta Mater.* **160**, 158–172 (2018).
- Eleti, R. R., Bhattacharjee, T., Shibata, A. & Tsuji, N. Unique deformation behavior and microstructure evolution in high temperature processing of HfNbTaTiZr refractory high entropy alloy. *Acta Mater.* **171**, 132–145 (2019).
- Wei, Q. et al. High-temperature ultra-strength of dual-phase $\text{Re}_{0.5}\text{MoNbW}(\text{TaC})_{0.5}$ high-entropy alloy matrix composite. *J. Mater. Sci. Technol.* **84**, 1–9 (2021).
- Wang, B. et al. Nitride-reinforced HfNbTaTiV high-entropy alloy with excellent room and elevated-temperature mechanical properties. *J. Mater. Sci. Technol.* **149**, 31–41 (2023).
- Guo, Y. et al. Strengthening and dynamic recrystallization mediated by Si-alloying in a refractory high entropy alloy. *Mater. Sci. Eng. A* **832**, 142480 (2022).
- Gou, X., Cao, R., Zhou, W., Shen, Z. & Li, Y. Microstructures, mechanical properties, and strengthening mechanisms of the $(\text{NbMoTa})_{100-x}\text{C}_x$ refractory medium-entropy alloys. *J. Mater. Sci. Technol.* **214**, 105–119 (2025).
- Wu, S. et al. Microstructure and mechanical properties of $\text{C}_x\text{Hf}_{0.25}\text{NbTaW}_{0.5}$ refractory high-entropy alloys at room and high temperatures. *J. Mater. Sci. Technol.* **97**, 229–238 (2022).
- Wan, Y. et al. Structures and properties of the $(\text{NbMoTaW})_{100-x}\text{C}_x$ high-entropy composites. *J. Alloy. Compd.* **889**, 161645 (2021).
- Sun, B. et al. Outstanding specific yield strength of a refractory high-entropy composite at an ultrahigh temperature of 2273 K . *J. Mater. Sci. Technol.* **166**, 145–154 (2023).

22. Wan, Y. et al. A nitride-reinforced NbMoTaW_{0.5}HfN refractory high-entropy alloy with potential ultra-high-temperature engineering applications. *Engineering* **30**, 110–120 (2023).
23. Senkov, O. N. et al. Microstructure and elevated temperature properties of a refractory TaNbHfZrTi alloy. *J. Mater. Sci.* **47**, 4062–4074 (2012).
24. Wang, Z. et al. Solving oxygen embrittlement of refractory high-entropy alloy via grain boundary engineering. *Mater. Today* **54**, 83–89 (2022).
25. Jia, Y. et al. Boron microalloying for high-temperature eutectic high-entropy alloys. *Acta Mater.* **262**, 119427 (2024).
26. Yang, T. et al. Ultrahigh-strength and ductile superlattice alloys with nanoscale disordered interfaces. *Science* **369**, 427–432 (2020).
27. Duan, F. et al. An order–disorder core–shell strategy for enhanced work-hardening capability and ductility in nanostructured alloys. *Nat. Commun.* **15**, 6832 (2024).
28. Wan, Y. et al. WReTaMo refractory high-entropy alloy with high strength at 1600 °C. *Adv. Eng. Mater.* **24**, 2100765 (2022).
29. Sun, B. et al. Promoted high-temperature strength and room-temperature plasticity synergy by tuning dendrite segregation in NbMoTaW refractory high-entropy alloy. *Int. J. Refract. Met. H* **118**, 106469 (2024).
30. Wan, Y. et al. Mechanical properties and phase stability of WTa-MoNbTi refractory high-entropy alloy at elevated temperatures. *Acta Metall. Sin.-Engl.* **34**, 1585–1590 (2021).
31. Liu, Y. et al. Microstructure and mechanical properties of refractory HfMo_{0.5}NbTiV_{0.5}Si_x high-entropy composites. *J. Alloy. Compd.* **694**, 869–876 (2017).
32. Wu, S., Qiao, D., Zhao, H., Wang, J. & Lu, Y. A novel NbTaW_{0.5}(Mo₂C)_x refractory high-entropy alloy with excellent mechanical properties. *J. Alloy. Compd.* **889**, 161800 (2021).
33. Senkov, O. N. et al. High-temperature mechanical properties and oxidation behavior of Hf-27Ta and Hf-21Ta-21X (X is Nb, Mo or W) alloys. *Int. J. Refract. Met. H* **96**, 105467 (2021).
34. Tan, Y., Ma, C. L., Kasama, A., Tanaka, R. & Yang, J. High temperature mechanical behavior of Nb–Mo–ZrC alloys. *Mater. Sci. Eng. A* **355**, 260–266 (2003).
35. Vegard, L. The constitution of mixed crystals and the space occupied by atoms. *Z. Phys.* **5**, 17–26 (1921).
36. Hua, Z. et al. Large hardening response mediated by room-temperature dynamic solute clustering behavior in a dilute Mg–Zn–Ca–Sn–Mn alloy. *Acta Mater.* **240**, 118308 (2022).
37. Hu, X. B. et al. Atomic configurations of various kinds of structural intergrowth in the polytypic M₂B-type boride precipitated in the Ni-based superalloy. *Acta Mater.* **100**, 64–72 (2015).
38. Hu, X. B., Zhu, Y. L., Sheng, N. C. & Ma, X. L. The Wyckoff positional order and polyhedral intergrowth in the M₃B₂- and M₅B₃-type boride precipitated in the Ni-based superalloys. *Sci. Rep.* **4**, 7367 (2014).
39. Zhu, Y. & Wu, X. Perspective on hetero-deformation induced (HDI) hardening and back stress. *Mater. Res. Lett.* **7**, 393–398 (2019).
40. Wu, X. & Zhu, Y. Heterogeneous materials: a new class of materials with unprecedented mechanical properties. *Mater. Res. Lett.* **5**, 527–532 (2017).
41. Lei, Z. et al. Enhanced strength and ductility in a high-entropy alloy via ordered oxygen complexes. *Nature* **563**, 546–550 (2018).
42. An, Z. et al. Negative mixing enthalpy solid solutions deliver high strength and ductility. *Nature* **625**, 697–702 (2024).
43. Bu, Y. et al. Local chemical fluctuation mediated ductility in body-centered-cubic high-entropy alloys. *Mater. Today* **46**, 28–34 (2021).
44. Hÿtch, M. J., Snoeck, E. & Kilaas, R. Quantitative measurement of displacement and strain fields from HREM micrographs. *Ultra-microscopy* **74**, 131–146 (1998).
45. Eleti, R. R., Chokshi, A. H., Shibata, A. & Tsuji, N. Unique high-temperature deformation dominated by grain boundary sliding in heterogeneous necklace structure formed by dynamic recrystallization in HfNbTaTiZr BCC refractory high entropy alloy. *Acta Mater.* **183**, 64–77 (2020).
46. Dong, L. R. et al. Borrowed dislocations for ductility in ceramics. *Science* **385**, 422–427 (2024).
47. Wu, Z., Bei, H., Pharr, G. M. & George, E. P. Temperature dependence of the mechanical properties of equiatomic solid solution alloys with face-centered cubic crystal structures. *Acta Mater.* **81**, 428–441 (2014).
48. Gou, S. et al. Additive manufacturing of ductile refractory high-entropy alloys via phase engineering. *Acta Mater.* **248**, 118781 (2023).
49. Lee, C. et al. Strength can be controlled by edge dislocations in refractory high-entropy alloys. *Nat. Commun.* **12**, 5474 (2021).
50. Maresca, F. & Curtin, W. A. Mechanistic origin of high strength in refractory BCC high entropy alloys up to 1900 K. *Acta Mater.* **182**, 235–249 (2020).
51. Huang, Z., Chen, F., Shen, Q., Zhang, L. & Rupert, T. J. Combined effects of nonmetallic impurities and planned metallic dopants on grain boundary energy and strength. *Acta Mater.* **166**, 113–125 (2019).
52. Wu, X. et al. First-principles determination of grain boundary strengthening in tungsten: dependence on grain boundary structure and metallic radius of solute. *Acta Mater.* **120**, 315–326 (2016).
53. Tran, R. et al. Computational study of metallic dopant segregation and embrittlement at molybdenum grain boundaries. *Acta Mater.* **117**, 91–99 (2016).
54. Razumovskiy, V. I., Divinski, S. V. & Romaner, L. Solute segregation in Cu: DFT vs. experiment. *Acta Mater.* **147**, 122–132 (2018).
55. He, F. et al. Design of DO₂₂ superlattice with superior strengthening effect in high entropy alloys. *Acta Mater.* **167**, 275–286 (2019).
56. Rice, J. R. & Wang, J. Embrittlement of interfaces by solute segregation. *Mater. Sci. Eng. A* **107**, 23–40 (1989).
57. Kim, J. et al. Low-dielectric-constant polyimide aerogel composite films with low water uptake. *Polym. J.* **48**, 829–834 (2016).
58. Lu, W. et al. New strategy in light-weight and ultrastrong Ti₄₀Nb₁₅Mo₃₀(NbC)₁₅ refractory complex concentrated alloy. *Composites Part B-Eng.* **281**, 111555 (2024).
59. Zhao, Y. Y., Chen, H. W., Lu, Z. P. & Nieh, T. G. Thermal stability and coarsening of coherent particles in a precipitation-hardened (NiCoFeCr)₉₄Ti₂Al₄ high-entropy alloy. *Acta Mater.* **147**, 184–194 (2018).
60. Yeh, J. W. et al. Nanostructured high-entropy alloys with multiple principal elements: novel alloy design concepts and outcomes. *Adv. Eng. Mater.* **6**, 299–303 (2004).
61. Stewart, J. Clark et al. First principles methods using CASTEP. *Z. Kristallogr.* **220**, 567–570 (2005).
62. Perdew, J. P., Burke, K. & Ernzerhof, M. Generalized gradient approximation made simple. *Phys. Rev. Lett.* **77**, 3865–3868 (1996).
63. Vanderbilt, D. Soft self-consistent pseudopotentials in a generalized eigenvalue formalism. *Phys. Rev. B* **41**, 7892–7895 (1990).
64. Monkhorst, H. J. & Pack, J. D. Special points for Brillouin-zone integrations. *Phys. Rev. B* **13**, 5188–5192 (1976).
65. Zunger, A., Wei, S. H., Ferreira, L. G. & Bernard, J. E. Special quasirandom structures. *Phys. Rev. Lett.* **65**, 353–356 (1990).
66. van de Walle, A. et al. Efficient stochastic generation of special quasirandom structures. *Calphad* **42**, 13–18 (2013).
67. Middya, T. R., Basu, A. N. & Sengupta, S. Self-consistent T-matrix solution for the effective elastic properties of perfectly disordered multiphase solids. *J. Appl. Phys.* **58**, 1809–1813 (1985).
68. Mao, H., Chen, H. & Chen, Q. TCHEA1: a thermodynamic database not limited for “high entropy” alloys. *J. Phase Equilib. Diffus.* **38**, 353–368 (2017).

Acknowledgements

This work is supported by the National Natural Science Foundation of China (No. 52231005 B.L.S., 52201174 Z.J.), the Jiangsu Provincial Key Research and Development Program (No. BE2021088 B.L.S.), Natural

Science Foundation of Jiangsu Province (No. BK20220858 Z.J.), the Guangdong Basic and Applied Basic Research Foundation (No. 2022A1515011402 L.G.S.), the Science, Technology and Innovation Commission of Shenzhen Municipality (No. GXWD20231130102735001 L.G.S., No. ZDSYS20210616110000001 L.G.S.), Development and Reform Commission of Shenzhen (No. XMHT20220103004 L.G.S.), and Jiangsu Key Laboratory for Advanced Metallic Materials (Nos. AMM2020A01, AMM2024A02 B.L.S., No. AMM2023B05 Q.Q.W.).

Author contributions

Q.Q.W., Z.J., X.B.L., and B.L.S. designed the research; B.S., B.J.W., and J.K. prepared and characterized the samples; G.S. conducted 3D-APT characterizations; L.G.S. carried out DFT simulations; B.S., B.J.W., J.K., Q.Q.W., Z.J., L.G.S., and B.L.S. analyzed the data and discussed the results; B.S., B.J.W., Q.Q.W., J.K., Z.J., L.G.S., and B.L.S. wrote the manuscript. All authors reviewed and contributed to the final manuscript.

Competing interests

The authors declare no competing interests.

Additional information

Supplementary information The online version contains supplementary material available at <https://doi.org/10.1038/s41467-025-66617-8>.

Correspondence and requests for materials should be addressed to Qianqian Wang, Xiubing Liang or Baolong Shen.

Peer review information *Nature Communications* thanks Eun Soo Park and Zhijun Wang for their contribution to the peer review of this work. A peer review file is available.

Reprints and permissions information is available at <http://www.nature.com/reprints>

Publisher's note Springer Nature remains neutral with regard to jurisdictional claims in published maps and institutional affiliations.

Open Access This article is licensed under a Creative Commons Attribution-NonCommercial-NoDerivatives 4.0 International License, which permits any non-commercial use, sharing, distribution and reproduction in any medium or format, as long as you give appropriate credit to the original author(s) and the source, provide a link to the Creative Commons licence, and indicate if you modified the licensed material. You do not have permission under this licence to share adapted material derived from this article or parts of it. The images or other third party material in this article are included in the article's Creative Commons licence, unless indicated otherwise in a credit line to the material. If material is not included in the article's Creative Commons licence and your intended use is not permitted by statutory regulation or exceeds the permitted use, you will need to obtain permission directly from the copyright holder. To view a copy of this licence, visit <http://creativecommons.org/licenses/by-nc-nd/4.0/>.

© The Author(s) 2025